GEOPHYSICS, VOL. 77, NO. 2 (MARCH-APRIL 2012); P. B23–B34, 21 FIGS., 3 TABLES.
10.1190/GEO2011-0194.1

Case History

Three-dimensional inversion of airborne time-domain electromagnetic data with applications to a porphyry deposit

Dikun Yang[1] and Douglas W. Oldenburg[1]

ABSTRACT

We inverted airborne time-domain electromagnetic (ATEM) data over a porphyry deposit in central British Columbia, Canada and recovered the 3D electrical conductivity structure. Full 3D inversion was required because of the circular geometry of the deposit. Typical analysis, which assumes a homogeneous or layered earth, produces conductive artifacts that are contrary to geologic expectations. A synthetic example showed that those misleading artifacts arise by assuming a 1D layered earth and that a 3D inversion can successfully solve the problem. Because of the computational challenges of solving the 3D inversion with many transmitters of airborne survey, we introduced a work flow that uses a multimesh strategy to handle the field data. In our inversion, a coarse mesh and a small number of soundings are first used to rapidly reconstruct a large-scale distribution of conductivity. The mesh is then refined and more soundings are incorporated to better resolve small-scale features. This strategy significantly speeds up the 3D inversion. The progressive refinement of the mesh also helps find the resolution limit of the data and an appropriate mesh for inversion, thus overcomputing on an unnecessarily fine mesh can be avoided. The final conductivity structure has features that emulate the expected geologic structure for a porphyry system and this substantiates the need and capability for working in 3D. However, the necessity for using 3D can depend upon the EM system used. A previous 1D interpretation of frequency-domain EM data at Mt. Milligan indicated a resistive stock. We reconciled this result with the present by computing the footprints of the frequency and time-domain surveys. The distribution of currents for the frequency-domain system was smaller than the length scale of the geologic target while the opposite was true for the time-domain data.

INTRODUCTION

Airborne time-domain electromagnetic (ATEM) surveying is a commonly used geophysical method for problems associated with mineral exploration, ground water and geologic mapping. Conventionally, ATEM data are interpreted by directly looking at time channel maps, profiles of multiple time channels, or carrying out 1D imaging or inversion. Widely adapted inversion and interpretation methods include apparent conductivity (Fraser, 1978; Palacky and West, 1991; Palacky, 1993), time constant analysis (Palacky and West, 1973; Macnae, 1998), conductivity depth transforms/imaging (Wolfgram and Karlik, 1995; Eaton, 1998; Macnae, 1998; Fullagar and Reid, 2001; Macnae et al., 2010), and inversions assuming a 1D layered earth model (Farquharson and Oldenburg, 1993; Lane et al., 2000; Wolfgram et al., 2003; Sattel, 2005; Brodie and Sambridge, 2006; Vallee and Smith, 2009; Fullagar et al., 2010). The difficulty with carrying out rigorous inversions in higher dimensions is the fact that Maxwell's equations must be solved for each transmitter. This dramatically increases the amount of computation as one transitions from 1D to 2D and then on to 3D.

Sometimes 2D and 3D inversions are made practical as parameter estimation problems, for example a typical model is one or multiple thin sheets buried in the host (Keating and Crossley, 1990; Raiche, 2004), but they are limited in applicability. Other software, like

Manuscript received by the Editor 3 June 2011; revised manuscript received 10 August 2011; published online 15 February 2012.
[1]University of British Columbia, Department of Earth and Ocean Sciences, Geophysical Inversion Facility, Vancouver, BC, Canada. E-mail: yangdikun@gmail.com; doug@eos.ubc.ca.

ArjunAir solving for a 2D model by using 3D source (2.5D), is also available for rigorous 2D inversion (Wilson et al., 2006).

With the advent of higher computing power and better algorithms it is now possible for the time-domain EM problem to be solved in 3D. Finite volume techniques (Haber et al., 2007; Oldenburg et al., 2008), finite-difference techniques (Commer and Newman, 2004; Newman and Commer, 2005) and integral equation techniques (Wilson et al., 2010; Cox et al., 2010) have been developed. Nevertheless, 3D inversion of ATEM data is still in its infancy with respect to routine application and there is much to be explored regarding when 3D is necessary and how best to carry out the inversion. Here we use the algorithm provided in Oldenburg et al., (2008) to carry out the inversion. The computations are made tractable for airborne data because the forward modeling matrix is factored and hence the equations can be solved efficiently when there are many right-hand sides.

There are two main goals for this paper: (a) to illustrate a specific geologic environment in which 3D inversion is necessary and to understand the details about why this is so, and (b) to show that the inversion can be carried out with relative efficiency if a thoughtful work flow is developed and implemented.

The paper proceeds as follows. We first outline the geologic background for the Mt. Milligan deposit, showing the airborne acquisition data, and 1D layered earth inversions and interpretations. The observed artifacts in 1D inversion are explained with the aid of 3D modeling and inversion of a synthetic example that emulates the deposit. We next focus on inverting the field data in 3D and how to speed up this process. We conclude with a short discussion regarding the 1D inversion of airborne frequency-domain and time-domain data at Mt. Milligan.

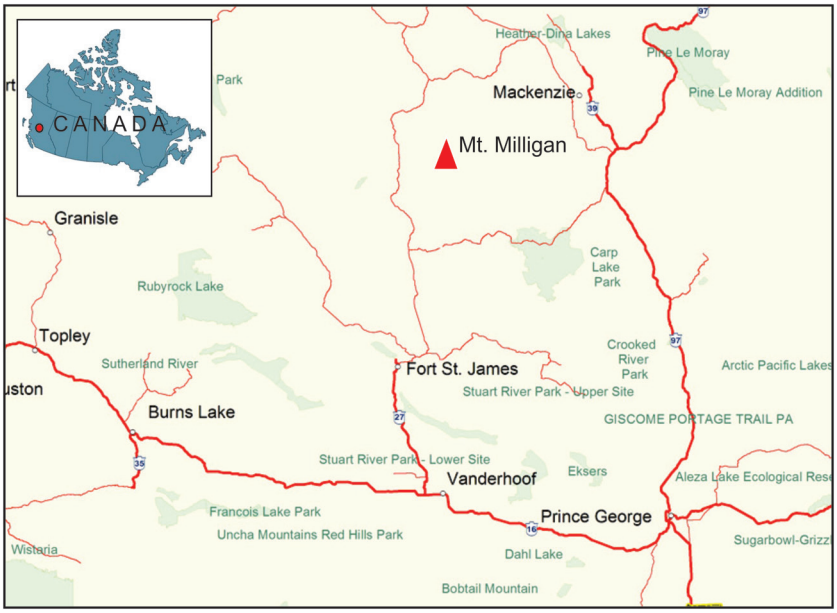

Figure 1. Geographic location of Mt. Milligan.

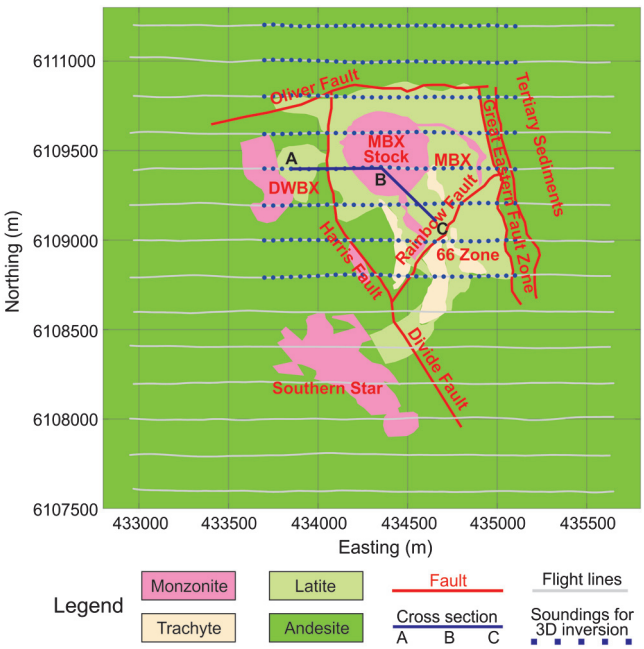

Figure 2. General geologic structure and ATEM flight lines at Mt. Milligan. Blue dots are the soundings involved in our 3D inversion. Location of the cross section in Figure 3b is indicated by A-B-C. The information in the map conveys the general geologic structure but it is not a true plan view section of the rock model at a specific depth.

GEOLOGIC AND PHYSICAL PROPERTY BACKGROUND

Mt. Milligan is an alkalic porphyry Cu-Au deposit situated approximately 155 km northwest of Prince George in north central British Columbia, Canada (Figure 1). The deposit was formed within the Early Mesozoic Quesnel Terrane, a Late Triassic to Early Jurassic magmatic arc complex that lies along the western North American continental margin where many similar porphyry deposits have been discovered in the past (Welhener et al., 2007).

Extensive exploration programs employing drilling, geologic, geochemical, and geophysical surveys have been carried out since the 1980s. Mt. Milligan consists of several mineralization zones of copper and gold (MBX, DWBX, 66 Zone, Southern Star in Figure 2). The mineralized zones are associated with monzonite stocks that have intruded into basaltic volcaniclastic rocks. Three types of alteration: potassic, albitic (sodic-calcic), and propylitic, are observed with a spatial geometry represented in Figure 3a. The region has also been tilted, and eroded so that the present MBX stock is dipping and cut by a fault at depth. The whole deposit is overlain by a layer of sedimentary overburden that becomes thicker on the east side because of the Tertiary sediments. Considerable drilling has been carried out and a 3D rock model has been composited. The alteration model, obtained by drilling around

MBX stock (Figure 3b), has a pattern similar to the theoretical model.

Despite extensive drilling, little logging for the electrical conductivity has been done, so the true conductivity model at the deposit scale is not available. However, there is still general information about conductivity that can be inferred from geologic and geophysical knowledge. There are basically four different geologic targets in terms of conductivity at Mt. Milligan (Figure 4). The most conductive unit is expected to be the overburden that is saturated or semi-saturated by ground water. Faults and fractured rocks are also likely to be conductive, especially when they are largely connected and serve as the pathway for ground water. On the other hand, solid and unaltered igneous rocks, whether intrusive or host, should be resistive. The alteration zone is the most complicated unit and its conductivity may vary over a broad range because of different types and degrees of alteration. In an attempt to obtain quantitative data of rock conductivity, Geoscience BC conducted laboratory conductivity measurements of hand samples from various porphyry deposits in British Columbia, including Mt. Milligan. The results are compiled in Figure 5 (Mitchinson and Enkin, 2011). Conductivity measurements show that the propylitically and albite-altered basalt can be relatively more conductive than other types of alteration due to high abundances of sulphides (pyrite and chalcopyrite). The monzonite, even altered, is still very resistive. Because ATEM is most sensitive to conductors, we expect that the ATEM survey at Mt. Milligan can delineate the overburden, water-saturated fractures and some conductive alterations that contrast with those resistive rock units, including potassically altered basalt, unaltered basalt and all types of monzonite.

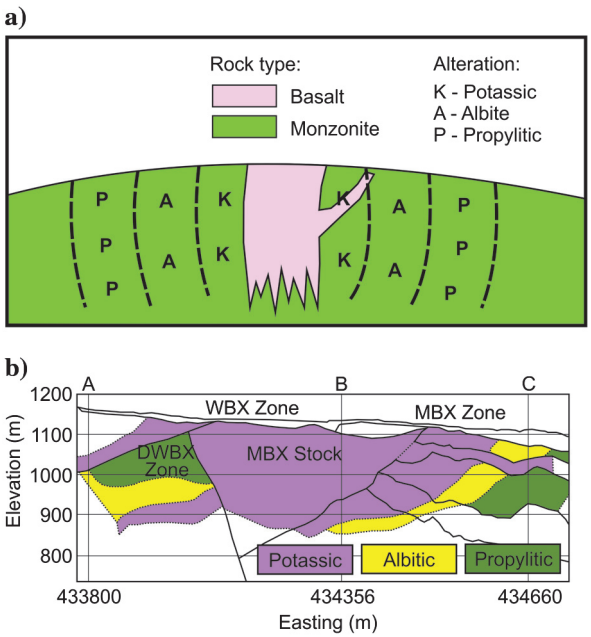

Figure 3. Cross section of porphyry system: (a) generic model with intrusive monzonite and surrounding alteration shells; (b) alteration model around the MBX stock at Mt. Milligan by Jago (2008), where potassic, albitic, and propylitic alterations shells are developed; location of this cross section (A-B-C) is indicated in Figure 2.

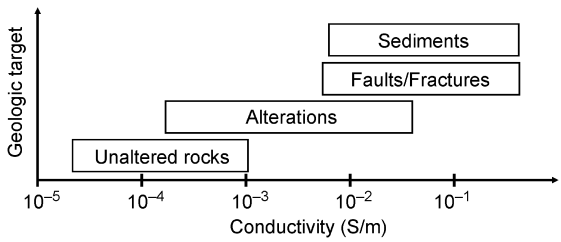

Figure 4. Conductivities of geologic targets at Mt. Milligan.

VTEM DATA OVER MT. MILLIGAN

In 2007, Geotech Ltd. carried out a versatile time-domain electromagnetic (VTEM) survey over the Mt. Milligan deposit as part of QUEST project initiated by Geoscience BC. The survey consisted of 14 lines, each 2.7 km long, with 200 m line spacing (gray lines in Figure 2). The VTEM survey covered all the mineralized zones

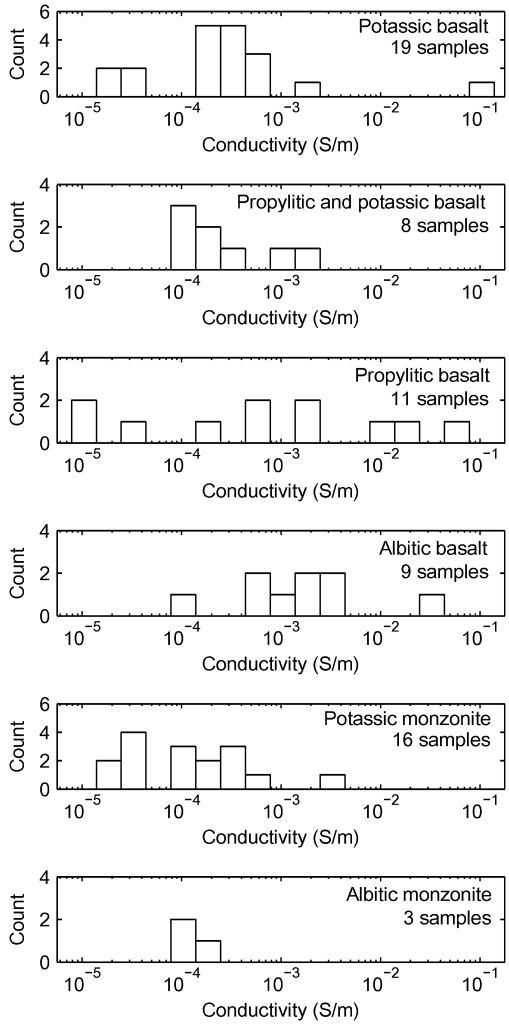

Figure 5. Histograms of the conductivity measurements of alteration hand samples from Mt. Milligan drill cores.

associated with the Mt. Milligan porphyry complex: MBX, DWBX, 66 Zone, and Southern Star.

The VTEM system (2007) has a transmitter loop of 13 m radius and dipole moment of 503,000 Am^2. The bird, including coincident transmitter and receiver, is towed about 42 m below the helicopter. The aircraft is positioned by onboard GPS and a radar altimeter. The system measures a voltage that is proportional to the time derivative of the vertical magnetic field (dBz/dt) in 27 off-time time channels from 99 to 9245 μs. These time channels are marked on the half-cycle of the transmitter current waveform in Figure 6. The VTEM system at Mt. Milligan has a base frequency of 30 Hz. In the final deliverables, the 30 waveforms per second are stacked (averaged) and then the data are filtered to give a reading every 3 to 5 meters along each traverse.

CONVENTIONAL METHODS OF ATEM DATA INTERPRETATION

There are several methods of interpreting ATEM data used routinely in the industry. Ideally, these methods provide useful information about the background conductivity, thickness of overburden, and identify anomalous regions that can be followed up. The methods produce an apparent conductivity, a time constant for the decay of the fields, and a 1D conductivity structure that fit the data.

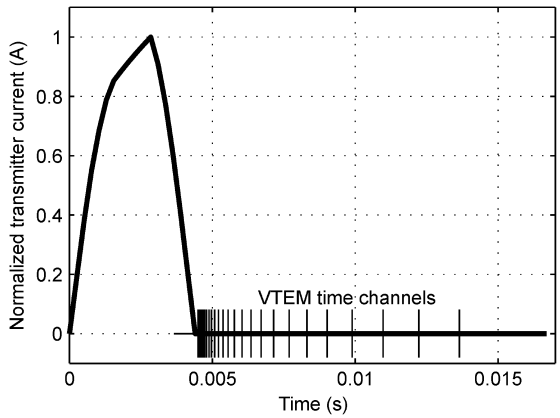

Figure 6. Transmitter current waveform and time channels of VTEM survey at Mt. Milligan.

Apparent conductivity is the conductivity of a uniform half-space that produces the same response as measured in a single time channel, or a best fit to a number of time channels. In this calculation, the flight height is taken into account. Here we use a look-up table similar to Sattel (2005) to rapidly find the half-space conductivity of a particular time channel at a certain height. If a solution is double-valued, the one minimizing lateral conductivity variation is chosen. Figure 7 shows an apparent conductivity map of the entire survey at 0.4 ms (VTEM time channel 9).

The time constant, or decay constant, τ, can provide a measure of the decay rate and is commonly used to rank conductors. It is estimated by fitting the transient signals with an exponential decay curve. For each sounding we computed a τ that best fits time channels $6 \sim 12$. These time channels correspond to the expected depth of deposit in this conductivity environment. The time constant map is shown in Figure 8.

In the third method, we invert the ATEM data to recover a 1D conductivity model for each sounding. While there are many 1D TEM inversion algorithms available, we use that outlined by Farquharson and Oldenburg (1993). For each sounding we seek a 1D model m that minimizes the objective functional

$$\begin{aligned}\mathbf{\Phi} &= \phi_d + \beta\phi_m \\ &= \|\mathbf{W}_d[\mathbf{F}(m) - d^{\text{obs}}]\|^2 \\ &\quad + \beta[\alpha_s\|\mathbf{W}_s(m - m^{\text{ref}})\|^2 + \alpha_z\|\mathbf{W}_z(m - m^{\text{ref}})\|^2]. \quad (1)\end{aligned}$$

In the equation above, ϕ_d is the data misfit, ϕ_m is the model norm or regularization functional, m is a vector of conductivities corresponding to layers with preset thicknesses, $\mathbf{F}$ is the forward mapping operator, $\mathbf{W}_d$ is a diagonal data misfit weighting matrix, d^{obs} is the observed data vector, β is a Tikhonov regularization parameter, α_s and α_z are user-prescribed weighting parameters, m^{ref} is the reference model, $\mathbf{W}_s$ is a diagonal weighting matrix, and $\mathbf{W}_z$ is a weighted first-order finite-difference operator. The regularization

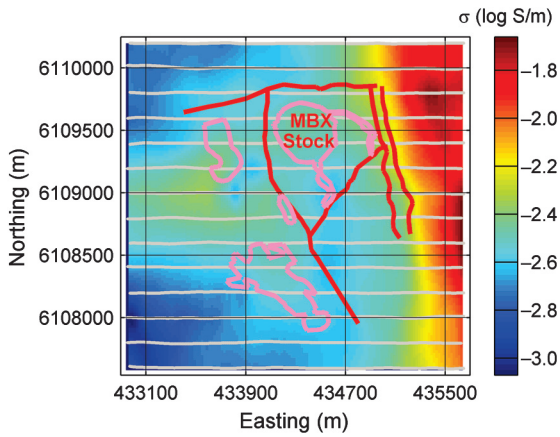

Figure 7. Apparent conductivity of VTEM survey at 0.4 ms at Mt. Milligan. Faults and monzonite stocks are outlined. Gray lines are survey lines.

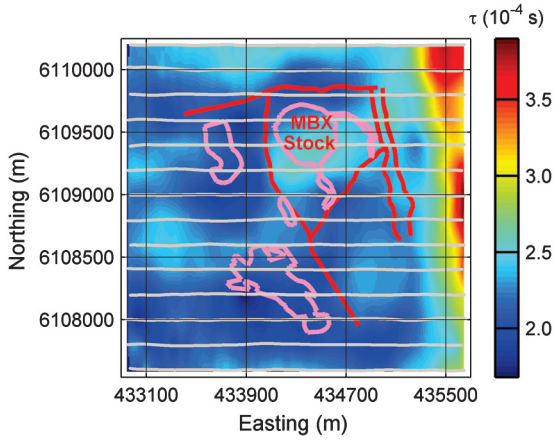

Figure 8. Time constant map at Mt. Milligan; data evaluated by VTEM time channels 0.234 ms ~ 0.682 ms. Faults and monzonite stocks are outlined. Gray lines are survey lines.

parameter is chosen so that the data are adequately fit. The optimization problem of minimizing equation 1 is solved with a Gauss-Newton method. In our 1D inversion, the top 600 m is subdivided into 40 logarithmically spaced layers. An uncertainty of 10% of the datum value plus a floor value of 10^{-13} V/A is assigned to each datum. The starting model for the 1D inversion at each sounding is the best-fitting half-space. The 1D models recovered from the inversion are stitched and interpolated to form a pseudo-3D volume of conductivity. Figure 9 shows the depth slice at elevation of 950 m.

Despite the differences in algorithms these three conventional ATEM data interpretation methods reveal very similar patterns of conductivity. In the large-scale there is good correspondence with regional geology, particularly the contrast between the conductive sediments on the east side and more resistive igneous rocks dominating the rest of survey area. There are similarities regarding smaller features, and in particular they all suggest that the conductivity associated with the MBX stock is higher than the host. This stock however is well-known to be monzonite and thus electrically resistive. In the following section, we will demonstrate that the misinterpretation arises from the assumption that the earth is 1D.

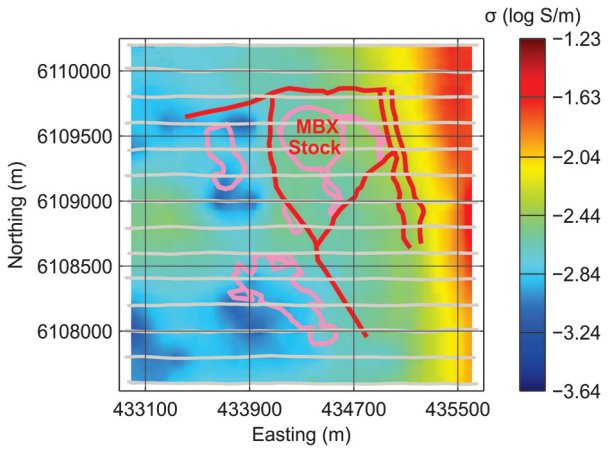

Figure 9. Depth slice of stitched 1D models at elevation of 950 m. Faults and monzonite stocks are outlined. Gray lines are survey lines.

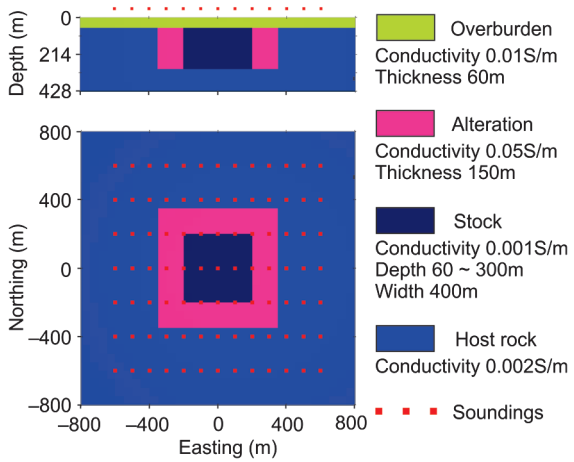

Figure 10. Synthetic model of conductivity at Mt. Milligan.

UNDERSTANDING THE 1D INVERSION RESULT

The high conductivity that coincides spatially with the location of the monzonite stock is a 1D interpretation artifact that arises because of 3D geometry. To show this we work with a synthetic porphyry-type model that consists of a thin conductive overburden overlying a resistive intrusive stock surrounded by a conductive alteration shell. The host rock is more conductive than the stock but less conductive than the alteration shell. The survey consists of 91 soundings at 50 m above the surface on a 7×13 data grid. This simulates an ATEM survey with 200 m line spacing and 100 m inline sounding spacing (Figure 10). The transmitter current waveform is a step-off. ATEM data are forward modeled at 20 VTEM time channels from 99 to 2745 μs using the algorithm in Oldenburg et al. (2008), which is a 3D finite volume forward code designed for solving the multisource time-domain EM problem by taking the advantage of a direct decomposition solver MUMPS (Amestoy et al., 2006).

The data are noise free but a 10% standard deviation is assigned to each datum for inversion. We first invert the data with the 1D inversion algorithm. The inversion parameters are the same as for the field data 1D inversion in the previous section. Figure 11 shows a cross section and depth slice of the pseudo-3D volume. The black wire frames outline the true model. The 1D inversion recovers the overburden but the remaining features are incorrect. There is a large conductor at the location where the resistive stock is supposed to be and the conductive shell is missing. The deep extension of the conductor on the cross section of Figure 11 also conveys very misleading information that the conductor is rooted at the depth of bedrock.

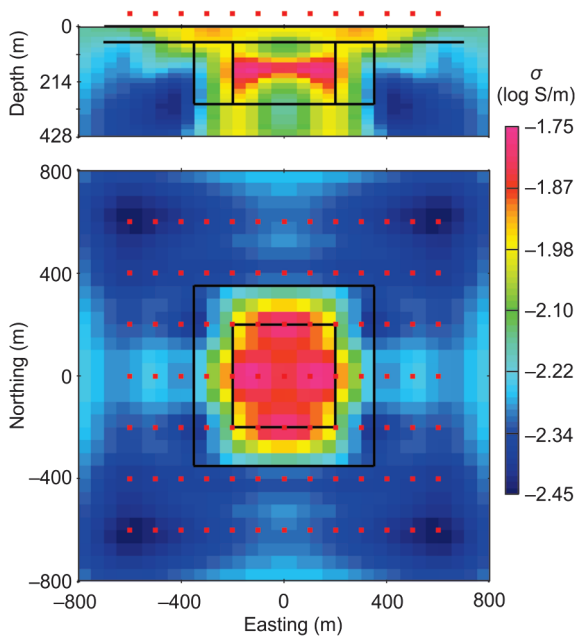

Figure 11. Central cross section (top) and depth slice 160 m below surface (bottom) of 1D synthetic inversion model. The true model is outlined by the black wire frames.

The above results are understood by looking at the currents and secondary magnetic fields in the earth at various times due to a transmitter located directly above the resistive stock. At early times, the induced currents are near the surface and localized beneath the transmitter (Figure 12a). Hence, a 1D inversion of the early time data should yield a reasonable estimate of the conductivity beneath the transmitter. However, at middle and late times, the currents propagate outward and downward and are concentrated in the conductive shell around the stock (Figure 12b). Once the currents reach the conductive material, they decay slowly in accordance with the local conductivity. These trapped currents produce significant dB/dt signals measured at the receiver and that signal can be translated into a conductivity high when the data are inverted in 1D.

The above phenomenon is well-known, and in fact forms the basic concept of why TEM surveys are useful. What was not appreciated before we undertook this analysis is how dramatic the effect can be. The circular geometry of the porphyry deposit and the location of the sounding maximizes the potential for a significant artifact, but other simulations, where the transmitter is displaced well away from the center of the deposit, produce a similar artifact. Once any appreciable amount of current reaches the conductive material, a significant signal will be generated at the receiver location.

Having now understood the weaknesses of interpreting the time-domain data in 1D, we proceed with 3D inversions of the synthetic and field data.

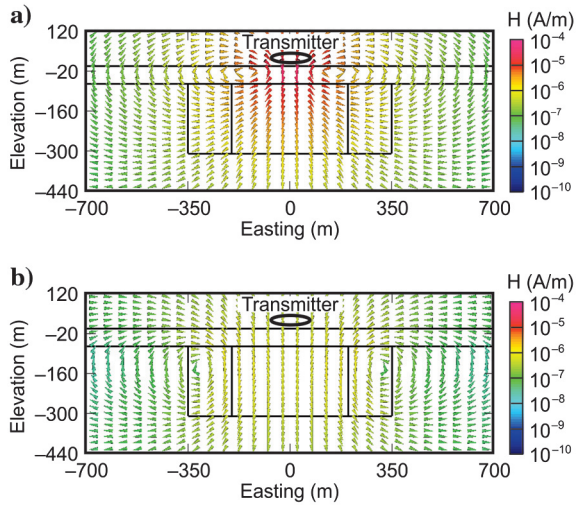

Figure 12. Snapshots of secondary magnetic field excited by a transmitter loop above the center of the resistive stock. Black wire frames outline the synthetic model in Figure 10. Currents are oriented perpendicular to the cross section plane. At early time, the currents are localized in the overburden close to the transmitter (a); at late time, the currents are mostly trapped in the conductive shell (b).

3D INVERSION OF MT. MILLIGAN SYNTHETIC MODEL

The inversion code used here is described in Oldenburg et al. (2008). The formulation of the inverse problem is similar to equation 1 for 1D, but with model norm components in three spatial directions and with the forward modeling extending to a 3D environment. Multisources are handled by factoring Maxwell's equations into a Cholesky decomposition. The overall efficiency of the inversion is dependent upon the time required for forward modeling and this is primarily controlled by the size of the 3D mesh, the number of factorizations of the Maxwell matrix, and the time for each factorization. Once factored, the time taken increases linearly with the number of transmitters (equivalent to soundings in ATEM). Efficiency motivates us to use as few cells and as few transmitters as possible, but we also need to keep small enough cells and enough soundings to get the resolution needed. Synthetic 3D inversion is a good format on which to explore these items.

We first design our mesh. For numerical accuracy, the smallest cell, $50 \times 50 \times 20$ m, is about one third of the diffusion distance of the earliest time for a 150 Ωm half-space. Padding cells are also needed so that appropriate boundary conditions are satisfied. The final mesh, $48 \times 48 \times 44$, consists of 101,376 cells. The uncertainty assignment is the same as for the synthetic 1D inversion shown in the previous section. Initial and reference models are uniform half-spaces of 200 Ωm. In anticipation of developing a strategy for solving large-scale problems using different numbers of soundings we carry out three individual inversions using 16, 49, and 91 soundings. The CPU times are summarized in Table 1.

Cross sections and depth slices of the three synthetic inversion models, and corresponding data misfit curves, are summarized in Figure 13. Even with only 16 soundings 400 m apart (Synthetic I in Figure 13a), the 3D inversion shows the conductivity contrast between the central resistive stock, the surrounding conductive shell and the host. The conductivities and geometry of anomalies are distorted, but the concept of a conductive shell around a resistive stock is evident. This contrasts with the incorrect image shown in Figure 11. Increasing the number of soundings to 49 in Synthetic II (Figure 13b) greatly improves the image. All three geologic units,

Table 1. Summary of three synthetic inversions using different numbers of soundings. All inversions are carried out on 3 nodes of computer cluster, with 6 Intel Xeon E5410 CPUs and 96GB RAM available.

Inversion	Number of transmitter	Sounding spacing (inline and crossline)	Number of β iterations	CPU time of factorization	CPU time of a forward modeling	Total CPU time of inversion
Synthetic I	16 (4×4)	400 m, 400 m	4	0:04:15	0:03:50	4:50:06
Synthetic II	49 (7×7)	200 m, 200 m	5	0:04:15	0:13:00	18:28:13
Synthetic III	91 (7×13)	100 m, 200 m	5	0:04:15	0:22:00	32:31:33

overburden, conductive shell, and resistive stock are correctly delineated and have more realistic conductivities. A further increase to 91 soundings in Synthetic III produces only marginal improvement by sharpening up the boundaries (Figure 13c). This improvement may not be justified by the increased computational time required for the inversion (see CPU time in Table 1).

To summarize, by carrying out synthetic 1D and 3D inversions we have learned that: (1) 3D inversion is necessary for geologic units with 3D geometry because 1D inversion can produce serious artifacts; (2) 3D inversion, even with a few soundings can still recover a reasonable large picture that outperforms a 1D inversion result; (3) there is a redundancy of information in the ATEM data, so an efficient inversion should strive to reduce the number of soundings involved while maximizing the amount of information from the data that can be incorporated into the model.

3D INVERSION OF MT. MILLIGAN VTEM FIELD DATA

For the Mt. Milligan VTEM field data we focus upon a 1.4×1.4 km region surrounding the MBX stock. The data are down-sampled to 50 m along lines, giving a total of 232 soundings on a 8×29 data grid (blue dots on gray lines in Figure 2). The 3D mesh has a horizontal cell size of 50 m which is the same as the inline sounding spacing; the smallest vertical cell size is 20 m, a value that is fine enough to capture the topography and accommodate the transmitter flight heights varying from 20 m to 90 m above surface. The final mesh is $50 \times 50 \times 64$ and has a total of 160,000 cells. The earliest time channels are often biased because of the cutoff effect of the primary field and thus we invert data from more stable time channels $6 \sim 20$. The assigned standard deviation for each datum is 10% plus a noise floor of 10^{-13} V/A; this is the same as our 1D inversion of Mt. Milligan VTEM field data. Discretization of the transmitter waveform is important because this affects the numerical accuracy, time, and memory usage when solving the forward problem. We discretize the waveform shown in Figure 6 to have a minimum number of partitions, each of which is discretized in a uniform Δt, and still retain desired accuracy. This results in two on-time and four off-time factorizations and a total of 50 time steps in one forward modeling.

With our current computer, the time for carrying out 50 time steps for 232 transmitters on a grid with 160,000 cells requires 33 minutes. Assuming an inversion based on the Gauss-Newton method typically requires 100 forward modelings and sensitivity-matrix-vector multiplications, we anticipate that an inversion would take about 50 hours. For practical purposes, it is desirable to reduce this value. One of the major factors for computation time is the number of cells. While a 3D mesh has to be fine enough to guarantee desired accuracy of the forward modeling and resolve small-scale features of the model, we note that a coarser mesh that moderately violates the general rules of spatial discretization may not hurt the model update at the early stage of 3D inversion because the data misfit is usually orders of magnitude greater than the discretization error. Likewise, including all the soundings in an early stage of inversion is not necessary and only a down-sampled subset is actually needed. We therefore propose a multimesh strategy to increase the efficiency of the large inversion problem. That is, first invert a small number of soundings on a coarse mesh, then pass the recovered model to a finer mesh and refine the model by inverting additional soundings. The last inversion is carried out on the finest mesh and includes all the soundings.

Our mesh design is guided by the concept of TEM diffusion distance (Nabighian and Macnae, 1991): the close-to-transmitter cells need to be smaller than half of the diffusion distance at earliest time over conductive ground and the padding zones need to extend at least two times of the diffusion distance at latest time over resistive ground. We choose 0.02 S/m and 0.001 S/m as the most conductive and the most resistive conductivity values at Mt. Milligan according to the 1D inversion. These give the maximum scale of close-to-transmitter cells about 70 m and the minimum padding

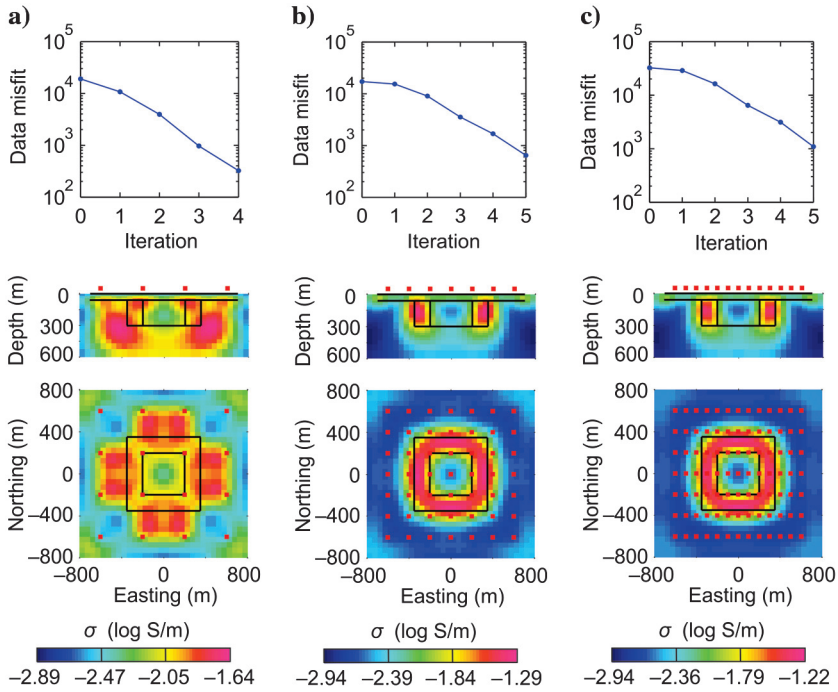

Figure 13. Data mist convergence and models of three synthetic 3D inversions. (a) Synthetic I with 16 soundings (b) Synthetic II with 49 soundings (c) Synthetic III with 91 soundings. Models are shown as cross sections (middle) and depth slices (bottom). The true model is outlined by black wire frames. Red dots indicate sounding locations.

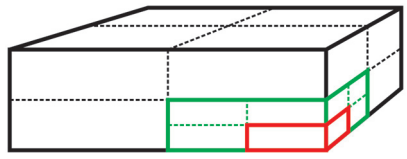

Figure 14. Dimensions of cells in the extracoarse (black), coarse (green) and fine (red) meshes.

distance about 4200 m. While keeping the inversion volume the same for all meshes, we design the dimensions of the smallest cells in the meshes to have an octree-like relationship as portrayed in Figure 14. For the current problem we use three meshes, which we refer to as extracoarse (X), coarse (C) and fine (F). The octree design reduces the size of the problem by factors of 8 and 64 on the coarse and extracoarse meshes and guarantees exact model conversion between meshes. Specifications of the extracoarse, coarse and fine mesh inversions are listed in Table 2.

Different meshes are used and numerical accuracy can be monitored by testing 3D forward modeled data against our 1D algorithm using conductive and resistive half-spaces. As shown in Table 3, all three meshes do well at late times over resistive ground because the same padding distance is used. However, modeling errors at early times increase as the mesh discretization becomes coarser. Poor modeling often creates artifacts in the inversion model, but fortunately those artifacts can be corrected in a subsequent finer mesh inversion. In addition, if the modeling error is excessive for early times then those time channels can be omitted from the inversion. Comparison of CPU time required by one forward modeling on the three meshes shows significant potential of speed-up by using coarser meshes in the early stages of the inversion.

We first implement the extracoarse mesh inversion on a Intel i7 960 Quad-Core desktop computer with 16GB RAM. The inversion starts with a 0.002 S/m half-space with topography and achieves a normalized data misfit 2.55 (blue curve in Figure 15) in about 1.73 hours (X-iterations in Figure 16). The model (X5) is converted to the coarse mesh and 100 m-spacing soundings are

Table 2. Specifications of the extracoarse, coarse, and fine mesh inversions.

Mesh	Smallest cell size	Number of cells	Sounding spacing (inline and crossline)	Number of soundings
Extracoarse	$200 \times 200 \times 80$ m	18,750	200 m, 200 m	64
Coarse	$100 \times 100 \times 40$ m	48,552	100 m, 200 m	120
Fine	$50 \times 50 \times 20$ m	160,000	50 m, 200 m	232

Table 3. Review of mesh performance. Modeling errors are evaluated by comparing data from a uniform half-space solution using a 1D code. CPU times are calibrated for one forward modeling on an Intel i7 960 Quad-Core desktop computer with 16GB RAM.

Mesh (Number of transmitter)	Modeling error of earliest time for a 0.02 S/m half-space	Modeling error of latest time for a 0.001 S/m half-space	Total CPU time of factorizations	Total CPU time of time steps
Extracoarse (64)	35%	3%	00:00:17	00:01:07
Coarse (120)	18%	3%	00:01:15	00:05:31
Fine (232)	6%	3%	00:12:14	01:02:02

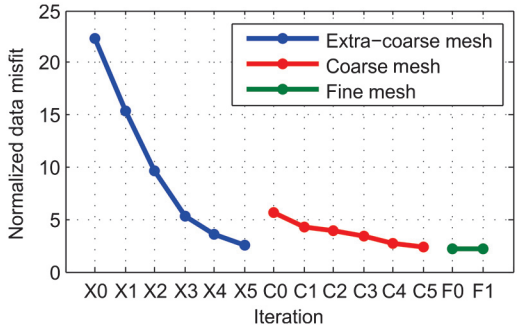

Figure 15. Normalized data mist as a function of iterations for inversions using three meshes. X, C, and F indicate extracoarse (blue), coarse (red), and fine (green) mesh inversions.

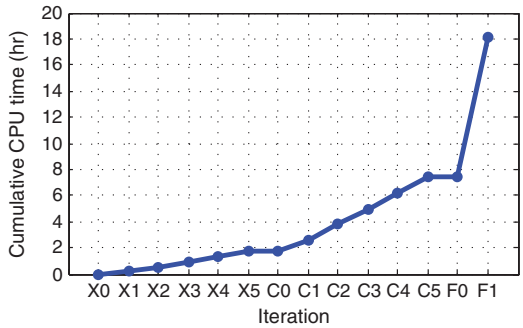

Figure 16. Cumulative CPU time of iterations in the extracoarse, coarse and fine mesh inversions. Note the extracoarse mesh inversion (X) is carried out on a Intel i7 960 Quad-Core desktop computer with 16GB RAM available; the coarse mesh inversion (C) on one node of a cluster with 2 Intel Xeon X5660 CPUs and 64GB RAM available; the fine mesh inversion (F) on two nodes of the same cluster with 4 Intel Xeon X5660 CPUs and 128GB RAM available.

used in the coarse inversion. Because of the information contained in those newly added soundings, the initial normalized data misfit of the coarse mesh inversion rises up to 5.72 (C0 in Figure 15). The coarse mesh inversion takes another 5.74 hours (C-iterations in Figure 16) to reduce the normalized data misfit to 2.32 (red curve in Figure 15). Finally, we convert to the fine mesh and use all of the soundings. However, these 50 m-spacing soundings do not provide significantly more information than the 100 m-spacing soundings. The initial normalized data misfit of the fine mesh inversion is 2.23 (F0 in Figure 15), which is even less than the final misfit of the coarse mesh inversion. The fine mesh inversion, which takes 10.65 hours for one iteration (F-iterations in Figure 16), is terminated when there is a reasonably good data fit; 80% of the data have normalized data misfit less than unity and there are only a few outliers that contribute large misfit (Figure 17).

Depth slices at elevation of 970 m of the three mesh inversion models (X5, C5, and F1) are shown in Figure 18. In spite of the substantial modeling error (Table 3), the extracoarse mesh does a good job of delineating the large-scale conductivity features over the entire area (Figure 18a). This inversion is carried out quickly on a desktop computer. Increased resolution is evident on the subsequent meshes. However, little difference is found between the coarse (Figure 18b) and fine (Figure 18c) mesh inversion models. This suggests that the 50 m-spacing data do not provide much more information than 100 m-spacing data and that the 100 m mesh would be fine enough for this data set. The total time to complete the inversion at the coarse mesh scale is 7.46 hours and the total time, with a fine scale mesh update, is 18.11 hours. These are significantly smaller than solving the problem on the fine scale from the beginning, which took 82.43 hours to achieve the same data misfit in a follow-up benchmark inversion.

GEOLOGIC INTERPRETATION

Depth slices of the final model are shown in Figure 19. The most conductive feature in this model is a near-surface conductor that cuts the northeastern corner, which is interpreted as the tertiary sediments. Our target, the porphyry system, is well-recovered as a deeply rooted massive resistor in the center of study area and a relatively conductive ring around it, with an opening toward the south. This feature can only be seen in the 3D inversion model and not in other methods or maps assuming a 1D earth model.

Figure 20a is a depth slice of the inversion model at elevation of 1030 m (about 100 m below the surface) with the geology overlaid. The general features are a resistive core, a surrounding conductive halo, followed by a resistive outer region. On the east, this sequence is modified by the presence of the highly conducting sediments. This conductivity model is also supported by previous 3D inversion of DC resistivity data (Oldenburg et al., 1997).[1] In Figure 20b we overlay contours of conductive anomaly from the DC resistivity inversion at the 1030 m elevation. There is general correspondence, especially for the west wing of the conductive ring and the shape of resistive stock.

We note that, in addition to the resistive stock which we have been focusing upon, there is a prominent dark-blue-colored resistor on the southern part of the image. This feature is required by the data which are characterized by unusual decay constants in that region. The cause of this is unknown and we are investigating its origin.

DISCUSSION

We have shown, with a synthetic example and field data inversion, that a 3D inversion of ATEM data is necessary if the geologic setting is similar to the Mt. Milligan porphyry deposit. The 1D inversions fail because of the lateral variation of the conductivity. However, in a previous study of Mt. Milligan (Oldenburg et al., 1997), 1D inversion of data from a different airborne EM system successfully revealed the resistive nature of the MBX stock. The survey was carried out with a frequency-domain loop-loop DIGHEM system. We attribute this paradox to the fact that the VTEM system, for the time channels used here, has a much larger footprint than the DIGHEM system. In this section we quantify the concept of footprint of an airborne EM system by using the distribution of

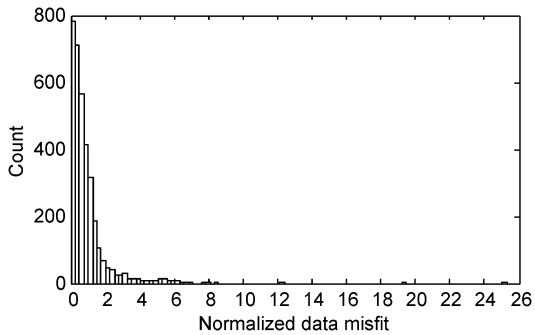

Figure 17. Histogram of normalized data mist after the fine mesh inversion. Total number of data is 3445 and almost 80% of data have achieved a normalized data misfit = 1.

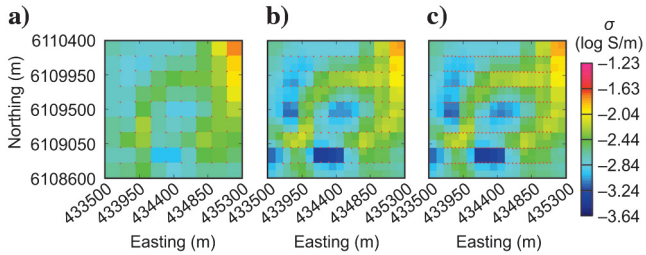

Figure 18. Depth slices of inversion models at elevation of 970 m after the (a) extracoarse, (b) coarse and (c) fine mesh inversions. Sounding locations are indicated by red dots.

[3]We provide a reference point for the conversion of coordinates system: 12400E, 9000N in the local grid in Oldenburg et al. (1997) = 433950E, 6109000N in the UTM coordinates used here.

electric current density, and then discuss the applicability of 1D inversion for airborne EM data.

In our investigation, we use the 3D inversion result of VTEM data as the conductivity model and place a transmitter loop above the center of the resistive MBX stock (transmitter location indicated by a red dot in Figure 21a). For the VTEM system, the transmitter current waveform is that shown in Figure 6. We forward model and compute the amplitude of the current density **J** in every mesh cell and for each time channel. To visualize the major current flows at a particular time, we set the cutoff threshold to be 10% of the peak amplitude of the current density for that time channel. For the DIGHEM system, the waveform is a sinusoid at three frequencies 56,000 Hz, 7200 Hz, and 900 Hz. The current density is calculated for each cell and a 10% cut-off threshold is also applied.

Figure 21b shows the cells with relatively large amplitudes of current density at the earliest time channel for our inversion (234 μs). The EM fields and associated currents have already reached the conductive halo surrounding the resistive stock. The large hole directly beneath the transmitter in Figure 21b is due to the lack of current inside the stock. At a later time, 1151 μs (Figure 21c), the EM field has diffused into a broader domain and the major current flow has spread further away. This illustrates that the off-time measurements of a VTEM system can have a footprint so large that conductive material, even far way from the transmitter/receiver location, has a large impact on the measured data. At the MBX stock, because of the low conductivity, we need a very sharp turnoff of the primary field and very early time channels to generate a footprint that is small enough to pick up the resistive feature of the stock.

The DIGHEM system, operating at relatively high frequencies and taking measurements while the primary field is present, has most of the contributing current flowing beneath the transmitter. At the two highest frequencies, the high current densities are observed primarily within the MBX stock (Figure 21d, 21e) and confined to a region that is inside the "hole" observed in Figure 21b. Even the lowest frequency still has a major current flow inside the stock (Figure 21f).

At Mt. Milligan, the size of our target, the MBX stock, is smaller than the footprint of VTEM system and is larger than, or equivalent to, the footprint of DIGHEM system. Therefore, the ground conductivity can be considered to be 1D at the scale of DIGHEM data and a 1D inversion is able to recover the correct local conductivity. At the scale of the VTEM data, the same conductivity structure becomes complex in three dimensions so that a 3D inversion with multiple soundings is needed.

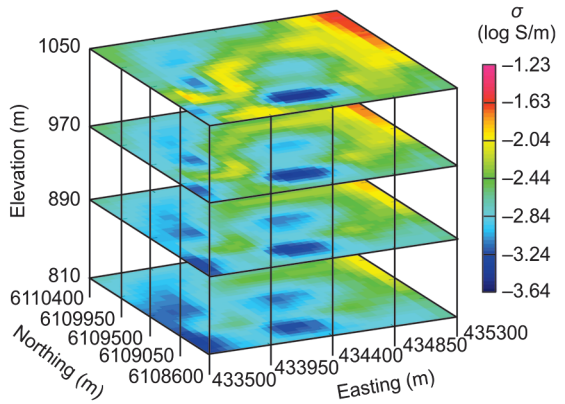

Figure 19. Depth slices of the final conductivity model at elevations 1050 m, 970 m, 890 m, and 810 m. Note the 3D structure of the circular conductor around the central resistive stock.

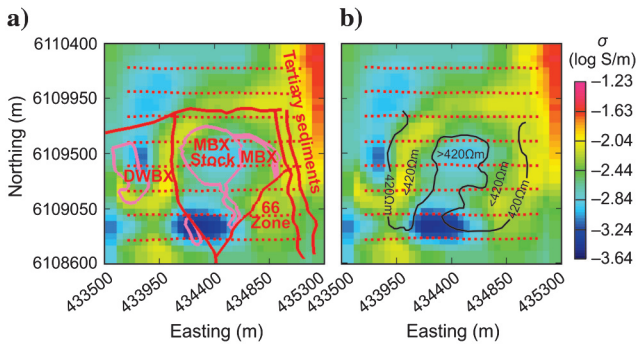

Figure 20. Depth slice of the final interpretation model at elevation of (a) 1030 m overlain by geology and (b) 420 m contour of DC resistivity model. The MBX stock is found resistive by 3D ATEM inversion and DC resistivity inversion.

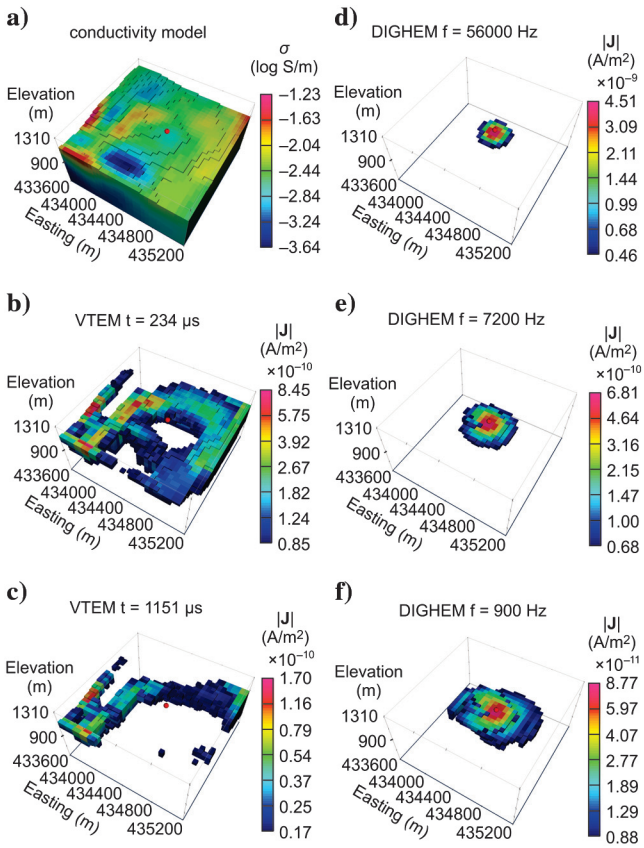

Figure 21. The footprints of the VTEM and DIGHEM systems. (a) conductivity model and location of the transmitter (indicated by a red dot); high current density cells with 10% cut-off threshold at (b) 234 μs the earliest VTEM time channel for inversion, (c) 1151 μs a midlate VTEM time channel, (d) 56,000 Hz of the DIGHEM system, (e) 7200 Hz, and (f) 900 Hz.

The difference in the footprints of the VTEM and DIGHEM is associated with two factors; the first concerns measurement times and operating frequencies of the system. If the time channels are early enough, or if the frequency is high enough so that the footprint is smaller than the scale of conductivity variation, then the local conductivity information can be picked up by an individual sounding and a 1D inversion can produce an interpretable result. However, for later time channels, or lower frequencies, the diffusion depths can exceed the scale of conductivity variation and a 3D inversion is necessary. The second element has to do with off-time versus on-time systems. For an off-time system the secondary field diffuses into the medium after the shutdown of the primary field and the measured secondary responses are primarily due to those currents well away from the transmitter. However, for a frequency system which is always on-time, the primary field has geometric decay that results in the strongest secondary field near the transmitter. It remains sensitive to the local conductivity, but it does look at progressively greater distances from the transmitter as the operating frequency lowers.

CONCLUSIONS

There are two main goals of this paper. The first is to show that traditional 1D analysis of ATEM data can lead to wrong interpretations and to understand the fundamental nature of why this is. The second is to illustrate that practical 3D inversions involving many transmitters can be carried out in a reasonable time by using a multimesh strategy. Both goals are achieved by working with airborne data from Mt. Milligan.

The deposit model at Mt. Milligan is well-known to consist of a central resistive core, and an outer conductive shell encased in a background volcanic host. For the time-domain system used here, all interpretation methods based upon the assumption that the earth is 1D will image the resistive monzonite stock as a conductive body. A synthetic example shows why this is so.

The solution to obtaining a realistic conductivity model is to carry out the inversion in 3D. The synthetic example shows this is possible and also that working with a reduced number of soundings and fairly coarse meshes can yield a result that captures the large-scale features of the model. Building upon this we implement a multimesh strategy for working with field data. We begin with a coarse mesh and a few soundings to generate the large-scale features and then progressively work with finer meshes and an increased number of soundings to obtain better resolution and better fits to the data. For the Mt. Milligan field data, we start with a 200 m-cell size and 200 m-spacing of the soundings, then 100 m-cell size and 100 m-spacing, followed by a final inversion with 50 m-cell size and 50 m-spacing. The full inversion of 232 transmitters for a mesh of 160,000 cells required only 18.11 hours on our system and effectively the same interpretation would have been achieved from the model obtained on an intermediate mesh after 7.46 hours. These times are significantly less than the 82.43 hours needed to carry out the inversion on the fine mesh.

The recovered 3D conductivity model clearly shows a central resistive stock and a surrounding conductor associated with alteration products. The result is also in general correspondence with the conductivity obtained by inverting DC resistivity data in 3D.

This study of the Mt. Milligan VTEM data has illustrated the need and our capability to invert ATEM data in 3D. Although the circular geometry at Mt. Milligan is tuned to producing artifacts in a 1D inversion, our experience has been that less extreme 3D environments can also result in significant misinterpretations when the scale of footprint of the system becomes large. For this reason, 3D inversion should become standard procedure for most ATEM data in mineral exploration. This requires increased computing power, which is becoming available, and also thoughtful work flows for implementing the inversion.

ACKNOWLEDGMENTS

The authors thank the members of the MITEM Consortium and NSERC for their financial support. D. Yang thanks Geoscience BC for the VTEM data at Mt. Milligan and for scholarships. The authors are also grateful to Peter Kowalczyk for a discussion which helped guide the investigation into the fundamental cause of the 1D TEM artifact. We also thank an anonymous reviewer for bringing to light the potential contradiction of results obtained by 1D inversion of frequency and time-domain data. This resulted in the analysis presented in the Discussion. We thank Terrane Metals Corp. for geologic background and for assisting our field trip to Mt. Milligan and we thank Dr. Dianne Mitchinson for providing the physical property measurements and for help with the geology.

REFERENCES

Amestoy, P. R., A. Guermouche, J. Y. L'Excellent, and S. Pralet, 2006, Hybrid scheduling for the parallel solution of linear systems: Parallel Computing, **32**, 136–156.

Brodie, R., and M. Sambridge, 2006, A holistic approach to inversion of time-domain air-borne EM: ASEG, Extended Abstracts,1–4.

Commer, M., and G. Newman, 2004, A parallel finite-difference approach for 3D transient electromagnetic modeling with galvanic sources: Geophysics, **69**, 1192–1202.

Cox, L. H., G. A. Wilson, and M. S. Zhdanov, 2010, 3D inversion of airborne electromagnetic data using a moving footprint: Exploration Geophysics, **41**, 250–259.

Eaton, P. A., 1998, Application of an improved technique for interpreting transient electromagnetic data: Exploration Geophysics, **29**, 175–183.

Farquharson, C. G., and D. W. Oldenburg, 1993, Inversion of time-domain electromagnetic data for a horizontally layered earth: Geophysical Journal International, **114**, 433–442.

Fraser, D. C., 1978, Resistivity mapping with an airborne multi-coil electromagnetic system: Geophysics, **43**, 144–172.

Fullagar, P. K., and J. E. Reid, 2001, Emax conductivity-depth transformation of airborne TEM data: ASEG, Extended Abstracts, 1–4.

Fullagar, P. K., J. Vrbancich, and G. Pears, 2010, Geologically-constrained 1D TEM inversion: ASEG, Extended Abstracts, 1–4.

Haber, E., D. W. Oldenburg, and R. Shekhtman, 2007, Inversion of time domain three-dimensional electromagnetic data: Geophysical Journal International, **171**, 550–564.

Jago, C. P., 2008, Metal- and alteration-zoning, and hydrothermal flow paths at the moderately-tilted, silica-saturated Mt. Milligan copper-gold alkalic porphyry deposit: M.S. thesis, University of British Columbia.

Keating, P. B., and D. J. Crossley, 1990, The inversion of time-domain airborne electro-magnetic data using the plate model: Geophysics, **55**, 705–711.

Lane, R., A. Green, C. Golding, M. Owers, P. Pik, C. Plunkett, D. Sattel, and B. Thorn, 2000, An example of 3D conductivity mapping using the TEMPEST airborne electromagnetic system: Exploration Geophysics, **31**, 162–172.

Macnae, J., 1998, Fast AEM data processing and inversion: Exploration Geophysics, **29**, 163–169.

Macnae, J., R. Mortimer, and K. Gilgallon, 2010, Deep conductor delineation through improved EMflow data processing: ASEG, Extended Abstracts, 1–4.

Mitchinson, D. E., and R. J. Enkin, 2011, Continued investigations of physical property-geology relationships in porphyry-deposit settings in the Quest and Quest-West project area, Central British Columbia (NTS 093E, K, L, M, N): Technical report, Geoscience BC.

Nabighian, M. N., and J. C. Macnae, 1991, Time domain electromagnetic prospecting methods, *in* M. N. Nabighian, eds., Electromagnetic methods

in applied geophysics, Applications, Part A and B: SEG, Investigations in Geophysics No. 3, Volume **2**, 427–520.
Newman, G., and M. Commer, 2005, New advances in three dimensional transient electromagnetic inversion: Geophysical Journal International, **160**, 5–32.
Oldenburg, D. W., E. Haber, and R. Shekhtman, 2008, Forward modelling and inversion of multi-source TEM data: 78th Annual International Meeting, SEG, Expanded Abstracts, 559–563.
Oldenburg, D. W., Y. Li, and R. G. Ellis, 1997, Inversion of geophysical data over a copper gold porphyry deposit: A case history for Mt. Milligan: Geophysics, **62**, 1419–1431.
Palacky, G. J.,1993, Use of airborne electromagnetic methods for resource mapping: Advances in Space Research, **13**, 5–14.
Palacky, G. J., and G. F. West, 1973, Quantitative interpretation of input AEM measurements: Geophysics, **38**, 1145–1158.
Palacky, G. J., and G. F. West, 1991, Airborne electromagnetic methods, *in* M. N. Nabighian, eds., Electromagnetic methods in applied geophysics, Applications, Part A and B: SEG Investigations in Geophysics No. 3, Volume **2**, 811–877.
Raiche, A., 2004, Practical 3D airborne EM inversion in complex terranes: ASEG, Extended Abstracts, 1–4.
Sattel, D., 2005, Inverting airborne electromagnetic (AEM) data with Zohdy's method: Geophysics, **70**, no. 4, G77–G85.
Vallee, M. A., and R. S. Smith, 2009, Inversion of airborne time-domain electromagnetic data to a 1D structure using lateral constraints: Near Surface Geophysics, **7**, 63–71.
Welhener, H. E., D. M. Labrenz, and J. Huang, 2007, Mt. Milligan project-resource report, Omenica mining district, British Columbia: Technical report, Independent Mining Consultants, Inc..
Wilson, G. A., L. H. Cox, and M. S. Zhdanov, 2010, Practical 3D inversion of entire airborne electromagnetic surveys: Preview, **149**, 29–33.
Wilson, G. A., A. P. Raiche, and F. Sugeng, 2006, 2.5D inversion of airborne electromagnetic data: Exploration Geophysics, **37**, 363–371.
Wolfgram, P., and G. Karlik, 1995, Conductivity-depth transform of GEOTEM data: Exploration Geophysics, **26**, 179–185.
Wolfgram, P., D. Sattel, and N. B. Christensen, 2003, Approximate 2D inversion of AEM data: Exploration Geophysics, **34**, 29–33.